Journal of the Electrochemical Society, **158** (11) D641-D646 (2011)
0013-4651/2011/158(11)/D641/6/$28.00 © The Electrochemical Society

Oxygen Incorporation into Electrodeposited CoFe Films: Consequences for Structure and Magnetic Properties

S. Elhalawaty,[a,b] R. W. Carpenter,[a,b,z] J. George,[c] and S. R. Brankovic[c,d,*]

[a]*Materials Science and Engineering Graduate Program, School for Engineering of Matter, Transport and Energy, and* [b]*LeRoy Eyring Center for Solid State Science, Arizona State University, Arizona 85287-1704, USA*
[c]*Electrical and Computer Engineering Department, and* [d]*Chemical and Biomolecular Engineering Department, University of Houston, Texas 77204-4005, USA*

The nanostructure and magnetic properties of electrodeposited $Co_{40}Fe_{60}$ alloy films containing varying amounts of oxygen were investigated using transmission electron microscopy (TEM) and diffraction, secondary ion mass spectroscopy (SIMS), and superconducting quantum interference device (SQUID) measurements. Oxygen content in the CoFe deposit was controlled by electrolyte composition. Films were deposited on Si {100} substrates with thin Cu/Ti seed layer. Electron energy loss and x-ray spectroscopies showed that the low oxygen films contained intragranular FeO particles and that the high oxygen films contained Fe_2O_3 along grain boundaries. The films with oxide present at the grain boundary had increased coercivity and reduced saturation magnetization relative to the lower oxygen content films with intragranular oxide. The differences in magnetic properties between low oxygen and high oxygen concentration films were attributed to stronger mobile domain wall interactions with the grain boundary oxide layers relative to interactions with the intragranular oxide particles in the low oxygen specimens.
© 2011 The Electrochemical Society. [DOI: 10.1149/2.011111jes] All rights reserved.

Manuscript submitted June 13, 2011; revised manuscript received July 25, 2011. Published October 5, 2011.

Fe-Co alloys have been extensively used in magnetic recording heads,[1] and high temperature applications such as gas turbine engines and magnetic bearings for high speed motors.[2] This is due to their soft ferromagnetic behavior, with high Curie temperature (~950°C), and high permeability associated with the very low magnetocrystalline anisotropy K_1 and low coercivity.[3] Additionally, near equiatomic CoFe alloys have the highest saturation magnetic flux density with B_S of 2.4 T among other soft magnetic alloys such as: Ni_{81} Fe_{19} (Permalloy) with B_S of 1.05 T, Ni_{45} Fe_{30} Co_{25} (Perminvar) with B_S of 1.55 T and Fe_{97} Si_3 with B_S of 2.01 T.[4]

The increase in areal density of magnetic recording brought many of the processes involved in fabrication of magnetic heads to the level of nanoscience, for instance: vacuum evaporation,[5] chemical vapor deposition,[6] thermal decomposition (Pyrolysis),[7] spin casting,[8] RF magnetron sputtering,[9,10] and electrodeposition.[11,12] One of the most promising ones to be used for future magnetic recording heads is electrodeposition.[13] It has been demonstrated that electrodeposition is capable of delivering high quality CoFe nanostructures with critical dimensions of ~40 nm to meet the design requirements of future magnetic recording heads.[14] Furthermore, electrodeposition allows fabrication of alloys with soft magnetic properties with relatively low capital cost and energy consumption requirements.[15] The magnetic properties of the deposited film are affected by synthesis parameters such as: current density, surface structure of the cathode (substrate), electrolyte composition, pH, and bath temperature, which all affect the film nanostructure, composition, and magnetic properties.[16]

In this study we investigate the effect of oxide/hydroxide incorporation into electrodeposited $Co_{40\text{-}36}Fe_{60\text{-}64}$ alloys on their structural and magnetic properties. The aim of this work is to gain more information about the state and quality of the oxide phase in electrodeposited $Co_{40\text{-}36}Fe_{60\text{-}64}$ alloys and to correlate its structure and origin to the composition of the electrolyte. In addition, the effort is made to establish relations between the observed magnetic properties of the $Co_{40\text{-}36}Fe_{60\text{-}64}$ films and the structure of the incorporated oxide/hydroxide phase (inclusions) and how these properties impacted the magnetoresistance of the deposited films. Further investigation regarding magnetoresistance will be presented in a separate publication. The $Co_{40\text{-}36}Fe_{60\text{-}64}$ films have been electro-deposited on Cu/Ti/Si substrates with different electrolyte compositions to incorporate oxygen; presumably as a separate oxygen rich phase in the films. The oxygen rich samples were produced from the electrolytes containing Fe^{3+} ions. In this case the main oxygen incorporation mechanism was through the precipitation of $Fe(OH)_3$ or $Fe_2O_3 \cdot xH_2O$ at the electrochemical interface, and its subsequent incorporation into the deposit during the film growth.[17] The low oxygen content samples were produced from the bath that did not have a significant Fe^{3+} presence; here the main oxygen incorporation mechanism was as a result of trapped anions (SO_4, BO_3) or from $Fe(OH)_2$ or $FeO \cdot xH_2O$ precipitates on the electrochemical interface during the film growth. Each oxygen source in the sample resulted in distinctively different structural and magnetic properties of CoFe films, which were studied in detail and are reported in this paper.

Experimental

For this study, a standard three electrode cell configuration with solution volume of 250 mL was used to electrodeposit $Co_{40\text{-}37}$ $Fe_{60\text{-}63}$ films (2.1 ± 0.2 μm thick) having different oxygen contents, denoted S1 and S2, on Cu (seed layer thickness 200 nm)/Ti (adhesion layer thickness 30 nm)/Si substrates. (100) Si wafer substrates were used to improve surface continuity and smoothness of the deposited films. Previously, different substrates have been used to deposit $Co_{40\text{-}36}Fe_{60\text{-}64}$ films, such as Cu and Al. However, surface quality was inferior to that of the films deposited on Si substrate. The electrodeposition was carried out under galvanostatic control. The aqueous solution compositions and electrodeposition parameters for both samples are described in Table I. For the higher oxygen content specimen, S2, the Fe^{3+} (0.0025M) was introduced into the electrolyte solution by adding 0.5 g/L of Ferric Sulfate $Fe_2(SO_4)_3 \cdot 4H_2O$, to introduce the additional amount of the oxide phase in the deposited film.[17] All solutions in this study were dearated for two hours before deposition experiments and during deposition experiments, in order to minimize additional formation of Fe^{3+} in the electrolyte through the oxygen reduction process ($4Fe^{2+} + O_2 + 4H^+ = 4Fe^{3+} + 2H_2O$).

Cross-sectional TEM samples were prepared using the focused ion beam (FIB) lift out technique. This technique was used to minimize the mass of ferromagnetic specimen material in the microscope objective lens pole piece gap, and thus minimize disturbance of images and spectra. Two wide trenches ($25 \times 8.7 \times 5$ μm) were milled at a current of 20 nA at 30 kV. Further thinning of the specimens on either side of usual the Pt strip was carried out at a reduced Ga ion current of 7 nA at 30 kV. Release cuts were made and the sample was "lifted-out" by welding it to a thin probe with deposited Pt, and then affixing it to a Cu grid, also by Pt deposition. The final thinning and cleaning up (removing amorphous surface layers) of both sides of the sample were achieved with ion beam currents of 0.5 nA at 30 kV and

* Electrochemical Society Active Member.
z E-mail: carpenter@asu.edu

Downloaded 13 Oct 2011 to 129.7.205.1. Redistribution subject to ECS license or copyright; see http://www.ecsdl.org/terms_use.jsp

Table I. Aqueous solution compositions and electrodepositing parameters.

Solution component	(g/L)	Process parameters	
$FeSO_4,7H_2O$	28	pH	2.01
$CoSO_4,7H_2O$	15	Current Density (mA/ cm^2)	4
H_3BO_3	25	Current Efficiency	0.56-S1 / 0.57-S 2
NH_4Cl	16	Deposition Rate (nm/min)	48
Saccharin	0.12	Deposition Time (min.)	40
		Stagnant Electrolyte	

1 nA at 5Kv, respectively. An electron beam maintained at 5 kV and a current of 1.6 nA was used for scanning electron microscopy (SEM) imaging in the FIB. Structure and composition characterization of the grown films were analyzed using a 200 keV TEM/scanning transmission electron microscopy (STEM)-2010F (JEOL, without aberration correction), equipped with a thin-window light-element-sensitive energy dispersive x-ray spectroscopy (EDS) and a Gatan Enfina electron energy-loss spectrometer (EELS).

Elemental depth profiles for Fe, Co, Cu and especially for H and O in the films were carried out by SIMS using a Cameca IMS-6f instrument with a Cs^+ primary ion beam at 10 keV and −9000V sample voltage (impact energy of 19kV), a beam diameter of 50–75 μm, and a beam current of 75 nA. The primary beam was rastered over 250 × 250 μm area. The magnetic properties of the CoFe films were determined using SQUID at room temperature.

Results and Discussion

A selected area electron diffraction (SAED) pattern for a cross section specimen of S2, presented in Fig. 1, showed that the crystal structure of CoFe was bcc with a weak ⟨111⟩ texture in the film plane. The inset shows a plan view SAED with inverted contrast for the same sample. The texture in a plan view sample was not as well defined as in cross-section specimens. SAED patterns displayed single phase spotty ring patterns with low background, indicating small grain size, and diffuse rings which are clearly visible in the inset. The diffuse rings could be attributed to the presence of an amorphous second phase in S2. The rings are near the d-spacing positions of (012), (110) and (116) planes in α-Fe_2O_3. S1 exhibited similar diffraction patterns with fewer and less intense diffuse rings than S2 due to less oxygen content present in S1, as discussed later. Figure 2a and 2b show a pair of TEM bright field (BF)/dark field (DF) images from S2. They revealed that the grain size ranged from 10–20 nm. Diffraction contrast images of S1 were essentially the same as S2. Figure 3 shows a typical high-resolution electron microscopy (HREM) image of S2. Both lattice and Moiré fringes are present, the latter because the grains are generally smaller than the foil thickness. The lattice spacing from both diffraction patterns and images agrees with those from $Co_{40\text{-}36}Fe_{60\text{-}64}$ alloys of our compositions.[18] There was no experimental evidence for a crystalline second phase. The same structure was found for S1.

From electrochemical deposition point of view, we expected two forms of oxides/hydroxides formed in the deposit during the electrolytic deposition. The main incorporation mechanism of the oxide/hydroxide in both samples is through the Fe-hydroxide precipitation. The Fe forms more insoluble hydroxide than Co and it is more likely to be incorporated in the film as a precipitate. In S1 sample, the form of Fe-hydroxide is $Fe(OH)_2$, while in S2 the dominant source of incorporated hydroxide is $Fe(OH)_3$. To elaborate further on this point we discuss the necessary conditions for Fe-hydroxide precipitation and incorporation in the $Co_{40\text{-}36}Fe_{60\text{-}64}$ films. These conditions are fulfilled when the pH level at the electrochemical interface (pH_i) exceeds the limit set by the product of solubility for particular Fe-hydroxide, as given by Eq. 1.[13,14,17]

$$pH_i > pH_{limit} = \frac{1}{n} \cdot \log \left\{ \frac{K_p}{[Fe^{n+}]_i \cdot (K_W)^n} \right\} \quad [1]$$

In above expression, the K_p, K_W and n stand for the product of solubility of particular Fe-hydroxide, ionic product of water and oxidation state of the Fe ion. The $[Fe^{n+}]_i$ term represents the concentration of the Fe ions at the electrochemical interface that are being incorporated into the hydroxide. For each sample, electrodeposition does not occur at transport limiting conditions because that concentration of the Fe^{2+} ions at the interface is approximately equal to the bulk concentration. The same applies for Fe^{3+} ions since they do not participate directly in the electrodeposition process.[17] The value of the pH_i is dependent on the parameters of the electrodeposition process such as pH of the solution, current density j, current efficiency γ, and diffusion layer thickness δ. The value of pH_i can be calculated from:[14,17]

$$pH_i = -\log \left\{ 10^{-pH} - \frac{j \cdot (1-\gamma)}{F} \cdot \frac{\delta}{D_{H^+}} \right\} \quad [2]$$

Taking the values of K_p for $Fe(OH)_2$ and $Fe(OH)_3$ as 4.87×10^{-17} $mol^3L^{-3}$and 2.79×10^{-39} mol^4L^{-4},[19] and the value of δ for stagnant

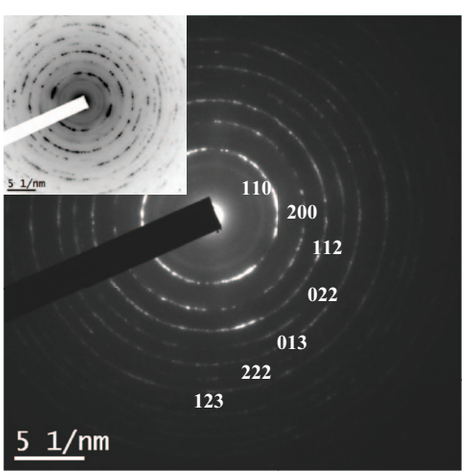

Figure 1. 200 keV cross sectional SAED pattern from CoFe film S2 showing a bcc crystal structure. Inset: plan view SAED, also from S2.

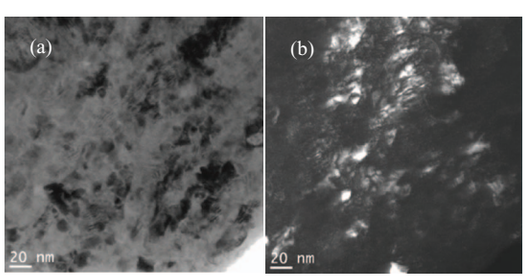

Figure 2. (a) BF and (b) DF for S2 showing the matrix grain size is 10 to 20 nm.

Downloaded 13 Oct 2011 to 129.7.205.1. Redistribution subject to ECS license or copyright; see http://www.ecsdl.org/terms_use.jsp

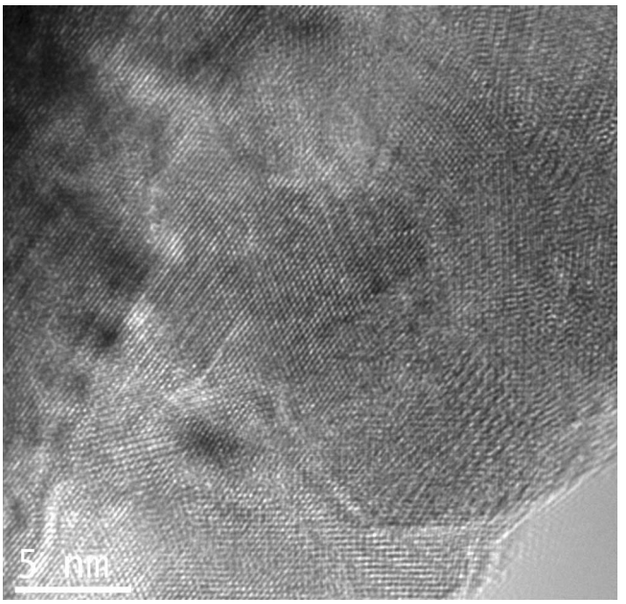

Figure 3. 200 keV HR image for S2. Note the frequent occurrence of Moiré fringes from overlapping nanocrystals.

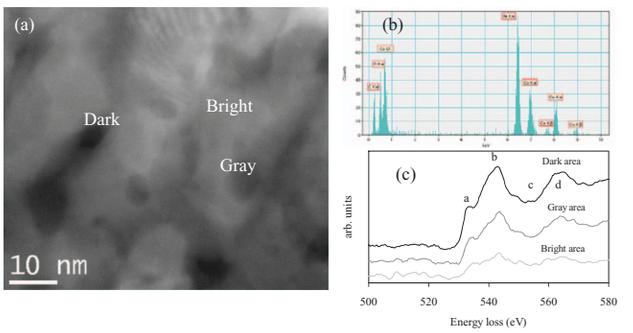

Figure 4. (a) 200 keV Z contrast STEM image for S1, (b) nanoEDS spectrum collected from dark area shown in Fig. 4a–4c O-K edge EELS spectra after background subtraction collected from areas shown in Fig. 4a. Note: a, b, c and d are characteristic peaks for O-K edge (see ref. 25 for further details).

electrolyte as $= 0.05$ cm[20] and having $D_{H^+} = 9.28 \times 10^{-5}$ cm^2 s^{-1},[21] it is easily shown that the pH_{limit} set by the right side of Eq. 1 is exceeded for both types of Fe-hydroxides during our deposition experiments ($pH_i = 6.7$ vs. $pH_{limit} = 6.3$ for $Fe(OH)_2$ and $pH_i = 3.8$ vs. $pH_{limit} = 2.02$ for $Fe(OH)_3$).

In S1 and S2, oxygen in the film could also come from entrapment of $\{SO_4\}^{2-}$ and $\{BO_3\}^{3-}$ ions, to produce one form of oxide phase A_xO_y with other elements trapped during electrodeposition process, such as S and B. Based on previous calculations, in S2, the predominant oxide phase was expected to be $Fe_2O_3 \cdot xH_2O$, which comes primarily from the introduction of Ferric Sulfate $(Fe_2SO_4)_3$ into the electrodeposition bath.[17,22] Accordingly, we expected S2 would have higher amount of oxide phase than S1 since the value of interfacial pH is significantly larger than the threshold required for precipitation of $Fe(OH)_3$ (Eq. 1).

Electron diffraction and phase contrast TEM imaging experiments did not reveal the expected presence of oxygen-containing second phases in these rather complicated nanostructures. Therefore, we performed compositionally sensitive atomic number (Z-contrast) STEM imaging combined with EELS and EDS to investigate further. Figure 4a shows a Z contrast image for S1 and it is clearly seen that there are some dark particles/regions within the small gains, corresponding to regions of weaker scattering, which could be regions of higher oxygen concentration (lower average Z). This possibility was confirmed by nanospectroscopy. Figure 4b shows one corresponding EDS spectrum collected with a 1 nm probe positioned at one of the dark regions of Fig. 4a. Other dark regions produced the same spectra.

The Fe/Co ratio was determined by the Cliff-Lorimer method.[23] In this case, the Cliff-Lorimer factor $k_{FeCo} \cong 1$ because the atomic weights, densities, cross sections and other parameters of Fe and Co are very nearly equal. The matrix Fe/Co atomic ratio was 1.7, which is consistent with the alloy composition $Co_{40\text{-}37}$ $Fe_{60\text{-}63}$, and the oxygen peak at 0.523 keV was very small. However, the Fe/Co ratio from the spectrum of the dark area shown in Fig. 4b was 2.6 and the oxygen peak was much larger. In these regions, where the oxygen was present in the film, the Fe content was enhanced relative to Co. In this specimen geometry the incident electron beam passes through a column of Fe-Co matrix above and below the dark particle. Keeping in mind that TEM images are 2D projections from 3D objects, these spectra are from composite specimens composed of columns of matrix with small particles in them. Using the foil thickness relative to particle size (typically 70 to 100 nm relative to 10 nm) at 200kV and the Fe/Co ratio ratios from matrix and with the probe on a particle (1.7 to 2.6) we calculated that true metal composition of the oxide particles was about 97%Fe/3%Co, so the particles are nearly all iron oxide with little cobalt. This is consistent with the higher thermodynamic stability of iron relative to cobalt oxides.[24] No S or B was detected in EDS spectra for S1 or S2 confirming that the oxygen in the Fe-rich regions is primarily bonded to Fe as Fe_xO_y. Figure 4c shows O K-edge EELS spectra, after background subtraction, collected from same areas shown in Fig. 4a. It is important to mention that the O K-edge, when bonded to Fe, is characterized by four distinctive sub peak positions which are labeled as a, b, c and d according to Colliex et al.[25] In this figure, the dark area has the largest O K-edge and the bright area has the smallest. This indicates that the darker the contrast the higher oxygen content. It is likely that the weak oxygen signal from the bright area is from a thin amorphous surface oxide, and not from oxygen incorporated during electrodeposition of the film. The O K-edge fine structure from the dark region corresponds to FeO oxide, according to the fingerprinting of Colliex et al.[25]

Figure 5a shows nanoEELS spectra collected from dark and bright areas shown in Fig. 4a. It is obviously seen that the Fe $L_{2,3}$-edge and O-K edge were prominent compared to Co $L_{2,3}$ edge for the dark area, whereas only a very weak O-K edge were detected in bright area. Figure 5b shows Fe L-edge EELS spectra, after background subtraction, collected from bright and dark areas. The Fe L-edge displays two prominent peaks labeled L_3 and L_2. They are referred to as white lines, due to transitions from the $2p_{3/2}$ and $2p_{1/2}$ levels to the unoccupied 3d states.[26] The change in the intensity of the L_3/L_2 ratio is correlated to a change in oxidation state of iron. The net integrated intensity ratio for the Fe L_3/L_2 edges increased from 1.45 in the bright matrix area to 1.8 in the dark oxygen-containing area. The ratio in bright matrix was consistent with the ratio we determined from a pure Fe sample. It is worthwhile to mention that bright and dark regions of S2 displayed the same trend as S1 in Figs. 5a and 5b.

Figure 6 shows a Z contrast image for specimen S2. The inset shows EELS oxygen concentration from a series of spectra along the line shown in the image, and the oxygen distribution shows a strong maximum at the grain boundary. The grain size in Z-contrast images was consistent with the TEM images in Fig. 2. Thus, the oxygen rich regions, which have a dark contrast compared to the CoFe matrix, were distributed along the grain boundaries in S2, rather than intragranularly as in S1. The small grain size and corresponding large grain boundary area imply that the oxygen/oxide content of S2 is larger than S1. It is worth mentioning that EDS spectra collected from matrix and across grain boundaries were similar to those collected from bright and dark areas in S1. So, there are oxygen rich regions in both samples which are bonded preferentially to Fe, as mentioned earlier, forming a separate phase in $Co_{40\text{-}36}Fe_{60\text{-}64}$ films. In order to

Downloaded 13 Oct 2011 to 129.7.205.1. Redistribution subject to ECS license or copyright; see http://www.ecsdl.org/terms_use.jsp

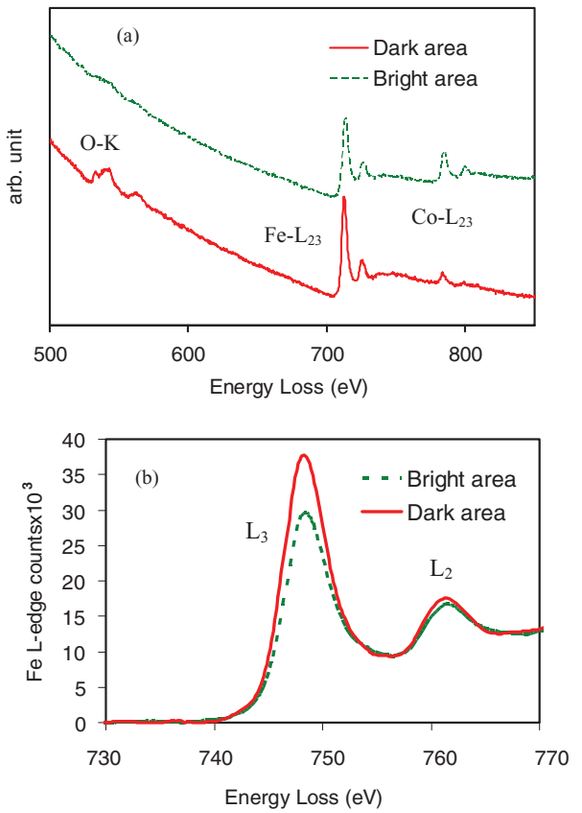

Figure 5. (a) O, Fe and Co edges EELS spectra (b) Fe L-edge EELS spectra after background subtraction, collected from bright and dark areas shown in Fig. 4b.

investigate the type of Fe oxide phase in both samples, the near edge fine structure (NEFS) of the O-K edge is useful. Different oxidation states of Fe give different O-K NEFS.

Figure 7 shows O-K edge NEFS for S1 and S2, taken from dark areas. The difference in the O-K edge onset peak between these samples suggests strongly that the dark regions along the grain boundaries in S2 are a form of α-Fe_2O_3 whereas in S1 the dark particles are FeO.[25] The white line ratio of Fe (L_3/L_2) increased from 1.8 in S1 to 2.2 in S2 due to higher valence state of Fe in S2, which correlates well with the information shown in Fig. 7.

SIMS results showed that the oxygen profile was nearly constant throughout the $Co_{40\text{-}36}Fe_{60\text{-}64}$ film thickness. Figure 8 shows the O^{18}/Fe^{56} ratio for S1 was ~ 0.13 compared to ~ 0.29 for S2, indicating that S2 had oxygen content about ~ 2.2 times higher than S1. This is consistent with our nanostructure analysis showing that oxygen in S1 was present as discrete intragranular particles with FeO type bonding, and that in the higher oxygen content S2 oxygen was present as a layer with α-Fe_2O_3 type bonding in $Co_{40\text{-}36}Fe_{60\text{-}64}$ matrix grain boundaries. We consider both the particles and the grain boundary oxides to be amorphous, since neither diffraction nor HREM provided much evidence for crystalline second phases. Hydrogen was detected during our SIMS analysis of both S1 and S2 films. This result is consistent with electrochemistry of the deposition process discussed above, and implies the oxygen-containing nanoregions we identified were iron hydroxides or hydrated oxides. The SIMS spatial resolution was insufficient to show that hydrogen was localized in the oxygen-containing particles we observed using electron microscopy.

The EELS 1s peak for hydrogen occurs at about 13 eV loss and is obscured by the zero-loss peak tail and other low-loss from the matrix, and therefore not detectable in our experiment. Most transition metal hydroxides and hydrated oxides undergo irradiation effect under 200

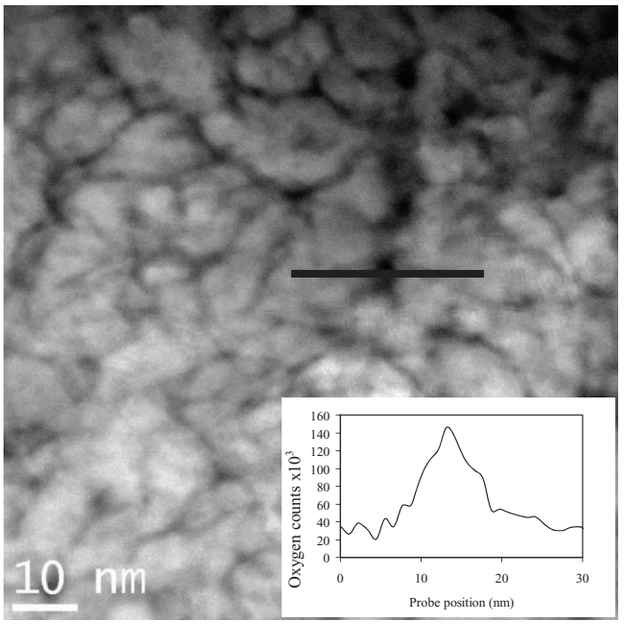

Figure 6. 200 keV Z contrast image for S2 shows line over which EELS spectra were collected. Inset: net O- K counts along the line shown in the image. The intensity is proportional to oxygen concentration along line scan. See text for details.

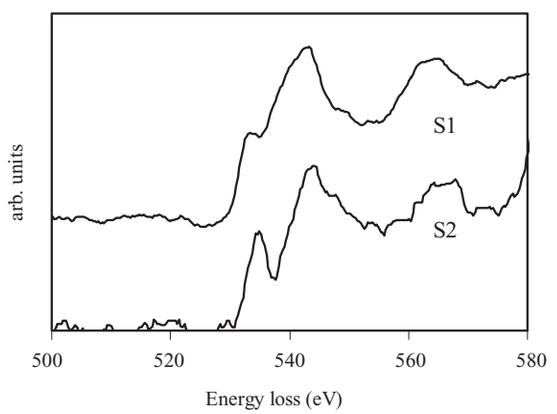

Figure 7. Background subtracted O K-edge from EELS nanospectra. The S1 spectrum is from dark particle in the matrix. The S2 spectrum is from a dark matrix grain boundary region. Note: the difference in edge onset structure.

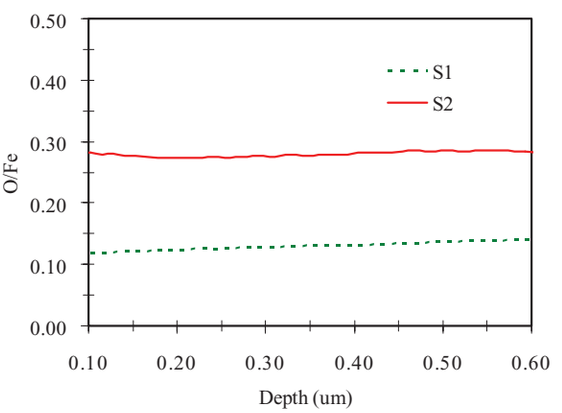

Figure 8. O/Fe ratio as a function of depth for S1 and S2 from SIMS measurements.

Downloaded 13 Oct 2011 to 129.7.205.1. Redistribution subject to ECS license or copyright; see http://www.ecsdl.org/terms_use.jsp

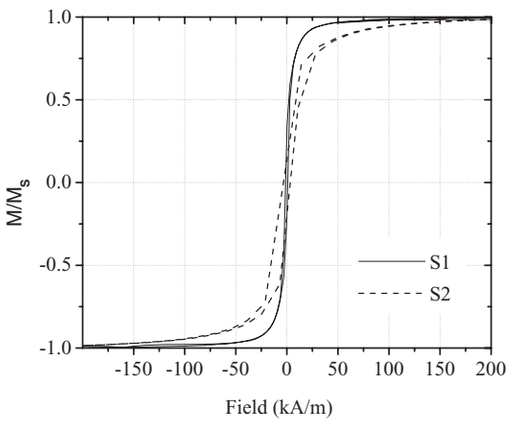

Figure 9. In- plane magnetic hysteresis loop of S1 and S2.

keV electron beam that result in structural disorder and loss of hydrogen and oxygen; these effects are dose dependent and visible in EELS spectra. Garvie[27] has shown that a transient peak, close to 530 eV loss (such as the threshold onset peak for S2 shown in our Fig. 7) appears early in the damage process and then disappears at larger electron doses. It is due to O_2 nanobubbles that form during irradiation. The peak disappears as O_2 from OH or H_2O leaves the specimen with increasing dose. However, in the case of anhydrous Fe_2O_3 (hematite) this peak is stable due to the oxide itself. For our work this peak was stable, so our electron microscopy results do not provide any direct evidence to determine whether our oxygen containing regions also contained hydrogen as implied by electrochemistry described above. Indirect evidence, such as the lack of crystallinity observed for our oxygen-containing particles, implies that radiation effects occurred, as one would expect for hydrogen and perhaps oxygen-containing particles. It is also possible that some of the hydrogen detected by SIMS was in the CoFe matrix itself, absorbed during the electrodeposition process or acquired by migration from the oxygen containing particles. Hydrogen is highly mobile in bcc Fe and its alloys even near room temperature ($D_H \approx 10^{-4}$ cm^2 s^{-1}) and segregates to lattice defects (such as grain boundaries, interfaces and dislocations) increasing its apparent solubility.[28,29] We conclude that the oxygen-containing nanoregions that we observed by TEM methods probably also contained hydrogen, either as water of hydration or hydroxyl ions.

Figure 9 shows the magnetization loops for S1 and S2 in the plane of the alloy films. S1 showed higher saturation magnetization and lower coercivity than S2. The measured magnetic properties of S1 and S2 are listed in Table II. Similar results and the same trend were also observed for 8 samples produced on different substrates such as Cu and Al. In both cases, S1 and S2, the saturation magnetization values are significantly smaller then what is expected for $Co_{40\text{-}36}Fe_{60\text{-}64}$ alloys of the same composition. Obviously, the oxide/hydroxide incorporation dilutes the magnetic moment of electrodeposited films. The simple argument based on volume partitioning of the electrodeposited films on the high value Ms magnetic phase ($Co_{40\text{-}36}Fe_{60\text{-}64}$) and weakly magnetic/antiferromagnetic or nonmagnetic inclusions ($FeO \cdot xH_2O$ or $Fe_2O_3 \cdot xH_2O$) is sufficient to explain this observation.[30] Coercivity of both films was larger than oxygen-free $Co_{40\text{-}36}Fe_{60\text{-}64}$ alloy of similar composition.[31,32] Since both films have similar grain size, the difference in coercivity cannot be attributed to a difference in grain size.[33] The difference in magnetic properties is governed by the presence of oxide phase in terms of its content, type and distribution. In the higher oxygen content specimen S2, the motion of domain walls was impeded more strongly by intergranular oxide phase than in S1, which contained intragranular oxide particles. Higher applied magnetic field was required to saturate S2. This is due to a difference in the exchange coupling energy between the grains depending upon the magnetic nature of the intergranular region.[34] There is also the possibility that processing of the $Co_{40\text{-}36}Fe_{60\text{-}64}$ films could have induced some magnetic anisotropy but we are not presently considering this complication in our analysis.

In general, one can invoke the inclusion theory to explain our magnetic properties observations, in which the separated regions of second phase with magnetic properties different from those of matrix act as magnetic inclusions. The magnetic inclusions (spherical regions) in S1 are likely supported by the Kersten model[35] where $H_C \alpha f^{2/3}$, where f is volume percent of second phase. However, the second phase in S2 can be considered as lamellar regions, with $H_C \alpha f$ based on the Goodenough model.[36] Thus, higher oxygen contents in S2 promote more pinning sites and a linear increase of coercivity with volume fraction of the second phase present in the film. The amount of saturation depends upon the magnitude of the magnetic moment of the atoms involved, and on the number of such moments per unit volume, which is determined by composition.[37] The M_s and H_C of S1 and S2 corresponded well with the oxygen content obtained from SIMS analysis.

Table II. Magnetic properties of S1 and S2.

Property	S1	S2	Units
Saturation mass magnetization	77	40	Am^2/kg
Coercivity H_C (in-plane)	1194	3342	A/m

Conclusion

Oxygen incorporation and the resulting oxygen rich phases in electrodeposited CoFe films have been studied. Z contrast STEM imaging combined with nanoEELS and nanoEDS confirmed the presence of oxygen rich regions in S1 and S2. EELS indicated the predominant oxide formed in S1 was $FeO \cdot xH_2O$, whereas in S2 was mainly $Fe_2O_3 \cdot xH_2O$. The difference in valence states of Fe in each oxide phase in these two samples indicates distinctively different sources and incorporation mechanisms. In the first case, oxygen incorporation from $Fe(OH)_2$ precipitation resulted in intragranular $FeO \cdot xH_2O$ in the alloy film. In the second case, addition of Fe^{3+} as $Fe_2(SO_4)_3$ to the solution resulted in precipitation of $Fe(OH)_3$ at the interface and incorporation of $Fe_2O_3 \cdot xH_2O$ lamellar particles in the alloy film grain boundaries. The distribution of two different oxides/hydroxides in the $Co_{40\text{-}36}Fe_{60\text{-}64}$ matrix of the sample S1 and S2 results in their different magnetic properties, i.e. coercivity. The Fe (III) oxide/hydroxide mainly distributed at the grain boundary areas, results in domain wall pinning and correspondingly higher coercitivity values for these samples. As oxygen content increased in $Co_{40\text{-}36}Fe_{60\text{-}64}$ film, the saturation magnetization decreased as expected from the relative increase in the volume fraction of nonmagnetic phase.

Acknowledgments

This work was supported by the NSF ECCS # 0824215. Use of facilities at Arizona State University is acknowledged. The authors are grateful to Prof. Ralph Chamberlin for helpful discussion.

References

1. P. C. Andricacos and N. Robertson, *IBM J. Res. Dev.*, **42**, 671 (1998).
2. R. H. Yu, S. Basu, Y. Zhang, and J. Q. Xiao, *J. Appl. Phys.*, **85**, 6034 (1999).
3. Z. Turgut, J. H. Scott, M. Q. Huang, S. A. Majetich, and M. E. McHenry, *J. App. Phys.*, **83**, 6468 (1998).
4. R. A. McCurrie, *Ferromagnetic Materials Structure and Properties*, p. 42, Academic Press (1994).
5. T. Hasiwa and M. Matsumoto, *IEEE Trans. Magn*, **24**, 2055 (1988).
6. P. Lane, B. Cockayne, P. Wright, and P. Oliver, *J. Cryst. Growth*, **143**, 237 (1994).
7. S. Eroglu, S. C. Zhang, and G. L. Messing, *J. Mater. Res.*, **11**, 1231 (1996).
8. L. Lagorce and M. Allen, *IEEE J. Microelectromech. Syst.*, **6**, 307 (1997).

Downloaded 13 Oct 2011 to 129.7.205.1. Redistribution subject to ECS license or copyright; see http://www.ecsdl.org/terms_use.jsp

9. T. Sakurai, O. Kitakami, and Y. Shimada, *J. Magn. Magn. Mater.*, **130**, 384 (1994).
10. M. Hanazono, S. Narishige, and K. Kawakami, *J. Appl. Phys.*, **64**, 2608 (1982).
11. C. Cheung, G. Palumbo, and Urb, *Scripta Metall. Mater.*, **31**, 735 (1994).
12. C. Chung, F. Djuanda, U. Erb, and Palumbo, *Nanostruct. Mater.*, **5**, 513 (1995).
13. S. R. Brankovic, X. M. Yang, T. J. Klemmer, and M. Seigler, *IEEE Trans. Magn.*, **42**, 132 (2006).
14. S. R. Brankovic, N. Vasiljevic, and N. Dimitrov, *Modern Electroplating V*, p. 573, M. Paunovic and M. Schlesinger, John Willey and Sons (2010).
15. Xiaomin Liu and Giovanni Zangari, *J. App. Phys.*, **87**, 5410 (2000).
16. M. Prutton, *Thin Ferromagnetic Films*, Butterworth, (1964).
17. S. R. Brankovic, S.-E. Bae, and D. Litvinov, *Electrochim. Acta*, **53**, 5934 (2008).
18. H. Okamoto, *Phase Diagrams of Binary Iron Alloys*, p. 97, ASM international, Ohio (1993).
19. D. R. Lide (Ed.), *CRC Handbook of Chemistry and Physics*, p. 8–119, 86th edition, Tailor & Francis, Boca Raton, FL (2005).
20. G. Prentice, *Electrochemical Engineering Principles*, p. 159, Prentice Hall, New Jersey (1991).
21. H. Schultz and M. Pritzker, *J. Electrochem. Soc.*, **145**, 2033 (1998).
22. S. R. Brankovic, J. George, S.-E. Bae, and D. Litvinov, *ECS Trans.*, **16**(45), 75 (2009).
23. G. Cliff and G. W. J. Lorimer, *Microsc*, **103**, 203 (1975).
24. James D. Coughlin, *Contribution to the Data on Theoretical Mettalurgy, XII Heat and Free Energy of Formation of Inorganic Oxides*, US Bureau of Mines, Bulltin 542, (1954).
25. C. Colliex, T. Manoubi, and C. Ortiz, *Phys. Rev. B*, **44**, 11402 (1991).
26. T. G. Sparrow, B. G. Williams, C. N. R. Rao, and J. M. Thomas, *Chem. Phy. Lett.*, **108**, 546 (1984).
27. Laurence A. J. Garvie, *American Mineralogist*, **95**, 92 (2010).
28. Paul Shewmon, *Diffusion in Solids*, 2nd edition, The Minerals, Metals, and Materials Society, Warrendale, PA (1989).
29. H. H. Johnson, *Met. Trans. A*, **19A**, 2371 (1988).
30. B. D. Cullity, *Introduction to Magnetic Materials*, p. 24, 152, Addison-Wesley Pub. Comp. London, UK (1972).
31. Carl Heck, *Magnetic Materials and their Application*, p. 388, Crane, Russak and Company, Inc., NY (1974).
32. Chin-Wen Chen, *Magnetism and Metallurgy of Soft Magnetic Materials*, p. 392, North-Holland, Amsterdam (1977).
33. Richard Boll, *Soft Magnetic Materials*, p. 24, Siemens-Aktiengesellscaft, London (1978).
34. Giselher Herzer, *Scripta Meta. Et Mat* **33**, Nos 10/11, 1741 (1995).
35. Ref. 32, p. 132.
36. John B. Goodenough, *Phys. Rev.*, **95**, 917 (1954).
37. Ref. 33, p. 20.

Downloaded 13 Oct 2011 to 129.7.205.1. Redistribution subject to ECS license or copyright; see http://www.ecsdl.org/terms_use.jsp